# Study on macro–micro mechanical behavior of rock like samples with hole and cracks

Dongmei Huang[1,2] · Shuyu Qiao[1,2] · Xikun Chang[1,3] · Xinzhao Wang[1,2] · Huanhuan Lu[1,2] · Xin Pan[1,2]

## Abstract

There are many holes and cracks in the rock, which significantly affect the strength of the rock mass. In this paper, the influence of holes and crack spacing on the uniaxial compressive strength and failure mode of rock samples with holes and cracks is studied. Through uniaxial compression testing, the macroscopic mechanical behavior of rock-like samples is summarized. Based on the experimental results, the microscopic parameters of the numerical model established in PFC$^{3D}$ are calibrated. Then, the uniaxial loading process is simulated to verify the numerical model. According to the simulation results, the influence of holes and crack spacing on the micro-failure mechanism of rock-like samples is analyzed from the perspective of mechanical properties, particle displacement, and failure mode. The results show that the uniaxial compressive strength and elastic modulus of the sample with holes are lower than those of the intact sample, but higher than those of the sample with single hole and double cracks. As the spacing between cracks increases, the peak strength and elastic modulus of the sample show a trend of first increasing and then decreasing. The maximum displacement of particles and the number of microcracks both show a trend of first increasing and then decreasing. During the loading process, there is a phenomenon of stress concentration on both sides of the hole and the crack tip, which can generate a large number of microcracks. Acoustic emission events can be divided into three stages: silent emission stage, stable stage, and rapid growth stage. The damage evolution process of the specimen can be divided into three stages: no damage stage, stable damage growth stage, and damage failure stage.

**Keywords** Hole · Crack spacing · Mechanical behavior · Mesoscopic damage

## 1 Introduction

In recent years, with the vigorous development of the economy, infrastructure construction such as architecture and transportation has entered a peak period. The construction

✉ Shuyu Qiao
202183200049@sdust.edu.cn

✉ Xikun Chang
skd994306@sdust.edu.cn

1 State Key Laboratory of Mining Disaster Prevention and Control Co-Founded By Shandong Province and the Ministry of Science and Technology, Shandong University of Science and Technology, Qingdao 266590, China

2 College of Safety and Environmental Engineering, Shandong University of Science and Technology, Qingdao 266590, China

3 College of Energy and Mining Engineering, Shandong University of Science and Technology, Qingdao 266590, China

scale and quantity are unprecedented, resulting in a large number of engineering projects such as rock tunnel excavation. During tunnel construction, various complex geological conditions will be encountered. With the action of dynamic loads, the development of external holes and cracks in the rock mass is particularly severe, posing a serious threat to the stability of the rock mass itself. In addition, rock masses in nature are influenced by complex geological structures, and there are a large number of primary cracks inside. Under the action of external forces, the primary cracks inside the rock mass will expand, grow, and even connect. This series of structural changes can trigger rock mass collapse accidents, causing serious economic losses and casualties. Therefore, it is of great significance to study the dynamic failure mechanism of rock with cracks and holes to ensure the smooth progress of geotechnical engineering.

The existence of crack and hole can significantly reduce the strength of rock mass, and they have great influence on rock stability engineering. In the past decades, many

compression tests have been carried out on rock materials with cracks, to study the crack propagation behavior and the strength variation induced by cracks. Because it is difficult to implant cracks in the original rock, and rock samples containing natural cracks are difficult to drill, researchers conducted experimental studies by preforming rock-like samples containing hole and cracks, etc. [1]. Huang et al. [2] prefabricated rocks containing single cracks, they found that the brittleness of the samples containing cracks decreased compared to the intact samples. Based on a large number of uniaxial experimental studies of parallel fractures, Huang et al. [3] prefabricated sandstone samples with non-parallel opening and penetrating fractures, and obtained that the stress–strain curve of intermittent fractured rock samples exhibits a multi-step softening. Based on the previous research on coplanar fractures, Wu et al. [4] analyzed the mechanical properties and crack evolution laws of non-coplanar discontinuous fractured rocks, and found that the rapid stress drop in the stress–strain curve is a macroscopic manifestation of crack propagation within the sample; Chen et al. [5] developed a rock crack directional propagation simulation device to investigate the effect of pre-crack size on the directional propagation of mode I cracks in rock; and Liu et al. [6] used 3D printing technology to prepare rock specimens with holes and double cracks. Through uniaxial compression tests, it was found that the uniaxial compressive strength (UCS) and elastic modulus of the specimens with holes and double cracks decreased compared to the specimens without holes and cracks; Wang et al. [7] used similar simulation materials to produce rock-like rocks with intersecting cracks. The study found that the compressive strength of samples with prefabricated cracks was significantly lower than that of complete test blocks. Most of the above studies are laboratory experiments. With the development of computer technology, more and more numerical simulation studies on rock crack evolution have been conducted [8–14]. Huang et al. [15] used the RFPA$^{2D}$ system to analyze the stress field characteristics and influencing factors of the static interaction of cracks, reproducing the superposition law of the stress field of the interaction of multiple cracks; Pan et al. [16] used EPCA$^{2D}$ to simulate the uniaxial compression fracture process of heterogeneous rock samples of different sizes, pointing out that when the homogeneity of rock samples is the same, the size and shape effects existing in the rock fracture process are caused by boundary loading; and Wang et al. [17] used the RFPA to study the impact of initial fracture angle on rock damage and fracture characteristics, and pointed out that the maximum value of the minimum principal stress increases fastest when the initial fracture angle is 15°. The simulation results reproduce typical experimental phenomena; Zhang et al. [18] carried out PFC$^{2D}$ simulation, analyzed the influence of rock strength on the energy evolution of coal and

rock structure, and proposed the zoning prevention and control method of roadway surrounding rock impact. He et al. [19] used digital image processing methods to analyze the mineral composition content and spatial distribution of granite, and analyzed the influence of mineral composition on the mechanical properties of granite through PFC$^{2D}$. They obtained the influence of quartz and feldspar on the uniaxial compressive strength, tensile strength, and elastic modulus of the sample, providing help for understanding the potential applications of granite mechanical behavior. He et al. [20] established a PFC$^{2D}$ numerical simulation model to analyze the evolution law and instability failure mechanism of crack initiation, propagation, and penetration in specimens with cross cracks. The variation relationship between the peak strength, elastic modulus, crack initiation stress, and crack inclination angle obtained from the numerical simulation results is basically consistent with the variation relationship between the indoor test results. A large number of studies have shown that numerical simulation can be used to further analyze the microscopical conditions inside samples, and the simulation results are reliable.

Due to the advantage of low stress concentration in circular tunnels compared to other shapes, a large number of railways and highways are generally constructed in the form of circular tunnels. In addition, there are a large number of primary cracks in the surrounding rock of the tunnel, and rocks containing one or more cracks are often encountered in engineering, and the cracks exist in parallel and intersection ways. This article aims to study the impact of railway and highway excavation on the stability of rock mass itself. Starting from the construction of rock mass engineering and based on extensive research on defective rocks, a circular tunnel is simplified as a through type hole, and on this basis, two parallel through cracks are considered. Rock-like samples with different positions of single holes and double cracks are prefabricated. Shimadzu AG–X250 electronic universal testing machine was used to carry out uniaxial compression test on the sample. The particle flow software PFC$^{3D}$ is used to simulate the uniaxial loading process of the samples. Based on the simulation results, this paper analyzes the influence of hole and crack spacing on the mechanical properties, acoustic emission properties, particle displacement, and failure mode of the model specimen. The failure mechanism and damage evolution of the sample were analyzed from a microscopic perspective.

## 2 Mechanical tests on damage and failure of rocks with holes and cracks

### 2.1 Specimen preparation

It is difficult to obtain ideal rock samples with cracks in field sampling and indoor processing. To obtain rock samples

with holes and cracks that can reflect the mechanical, deformation, and failure characteristics of the original rock, the physical similarity simulation method is usually used. The rock-like material used in the experiment selected river sand screened by 20-mesh sieve as the aggregate, the cementing agent was 425 cement, and the plastic influence agent was water. The mixture was made according to the mass ratio of $M_{water}:M_{cement}:M_{river\ sand} = 2:5:5$.

All components of the rock-like sample mold are made of acrylic material. The internal size of the mold is: length × width × height = 50 mm × 50 mm × 100 mm. The model picture and size are shown in Fig. 1. In order to obtain the rock-like specimen with cracks and holes in the specified position, cracks and holes were cut at the designated position of the mold by laser cutting method before the test. In the process of specimen pouring, steel sheet and round tube were embedded. The size of steel sheet was length × width = 100 mm × 10 mm, the thickness was 2 mm, and the diameter of round tube was 10 mm. Design a test rock sample with holes and four types of cracks with holes located in the center of the sample and a diameter of 10 mm. The distance of the two through cracks is 20, 30, 40, and 50 mm, respectively, the length of the cracks is 10 mm, the width is 2 mm, and the dip angle is 45°.

The preparation process of rock-like materials is divided into three basic steps: preparation of rock-like materials, installation of molds, and specimen maintenance, as shown in Fig. 2. Firstly, mix the cement, river sand, and water according to the predetermined ratio in the NJ-160A cement slurry mixer. Then, put the evenly mixed material into the mold and place it on the GZ-85 cement mortar vibration table, fully compacting and forming it. Finally, use a scraper to flatten the surface of the sample, let it stand for 24 h, and then demold it. Then, place the rock-like sample in the YH-60B standard constant temperature and humidity curing box for 28 days.

## 2.2 Uniaxial compression experimental

Shimadzu AG-X250 electronic universal testing machine was used to carry out uniaxial compression test on rock-like samples [21]. In order to reduce the impact of loading rate on the failure of rock-like specimens during the loading process, this experiment adopts a displacement loading control loading method and automatically collects test data through a computer. The loading rate was 0.01 mm/s. The sensitivity was set to 1% which means that the loading stress drops to 1% of the peak stress, the test automatically stops, and the complete stress–strain curve of the rock-like sample during the entire loading process is obtained. The equipment used in the experiment is shown in Fig. 3 [22, 23].

## 2.3 Experimental results

### 2.3.1 Mechanical attribute analysis

Through uniaxial compression experiments, the stress–strain curves of rock-like samples were obtained, as shown in Fig. 4. In the figure, 1-1 is a complete rock-like sample, 2-1 is a rock-like sample with single pores, and 3-1, 2, 3, and 4 are rock samples with double fractures single pore and gaps of 20, 30, 40, and 50 mm, respectively. Taking the 1-1 intact rock sample as an example, analyze the different stages of its pre-peak stress–strain curve:

(1) Compaction stage (oa stage): Due to the manual preparation of the sample, there are small pores or cracks inside the sample. These pores and cracks will be compacted during loading, with small stress changes and large strain changes. The stress–strain curve shows a concave shape and is nonlinear deformation.

(2) Elastic deformation stage (ab stage): In this stage, the original pore cracks of the sample are basically compressed and compacted, and the interior tends to stabilize. As the loading progresses, the stress–strain curve is almost linear, and the relationship between stress and strain is linear. There are no obvious cracks on the surface of the sample.

(3) Stable development stage (bc stage): As the loading progresses, obvious cracks begin to appear on the surface of the sample. The stress–strain curve shows a nonlinear upward convex growth trend. The growth trend slows down compared to the elastic deformation stage. The deformation occurring in this stage is mainly plastic deformation.

Analyze the peak strength and elastic modulus of six samples, as shown in Fig. 5. It can be seen that compared to the intact sample, the presence of holes significantly reduces the uniaxial compressive strength of the sample, but is higher than the peak strength of the sample with single hole and double cracks. The trend of change in elastic modulus is consistent with the trend of change in peak stress.

Further revealing the relationship between crack spacing and peak stress, the peak strain parameters of indoor tests on rock-like specimens with different cracks spacing were plotted as scatter plots and fitted, as shown in Fig. 6. It can be seen that under the experimental conditions, the yield point (peak value) first increases and then decreases with the increase in the distance between the two cracks, and the relationship between them meets the cubic function. The fitting equation shows a cubic function relationship between peak stress and crack spacing, which can be expressed as follows:

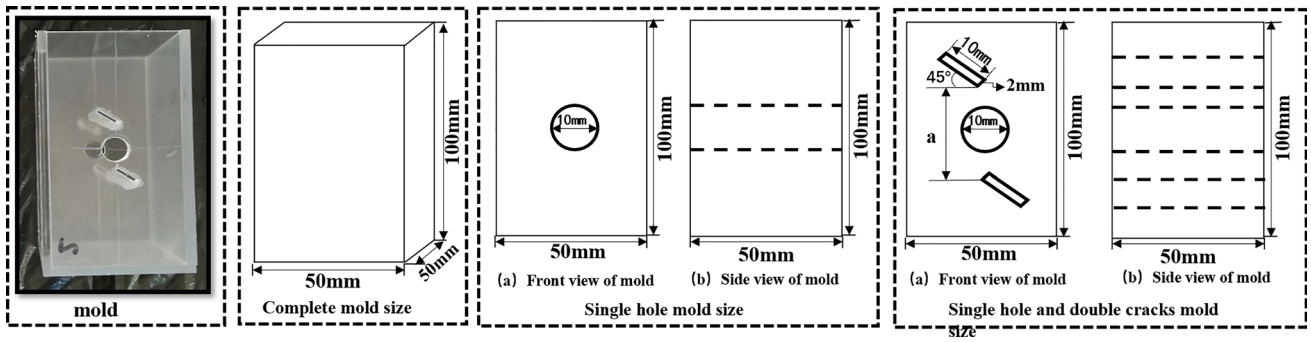$$Y = -36 + 4.00333x + -0.0915x^2 + 6.1667e^{-4}x^3 \qquad (1)$$
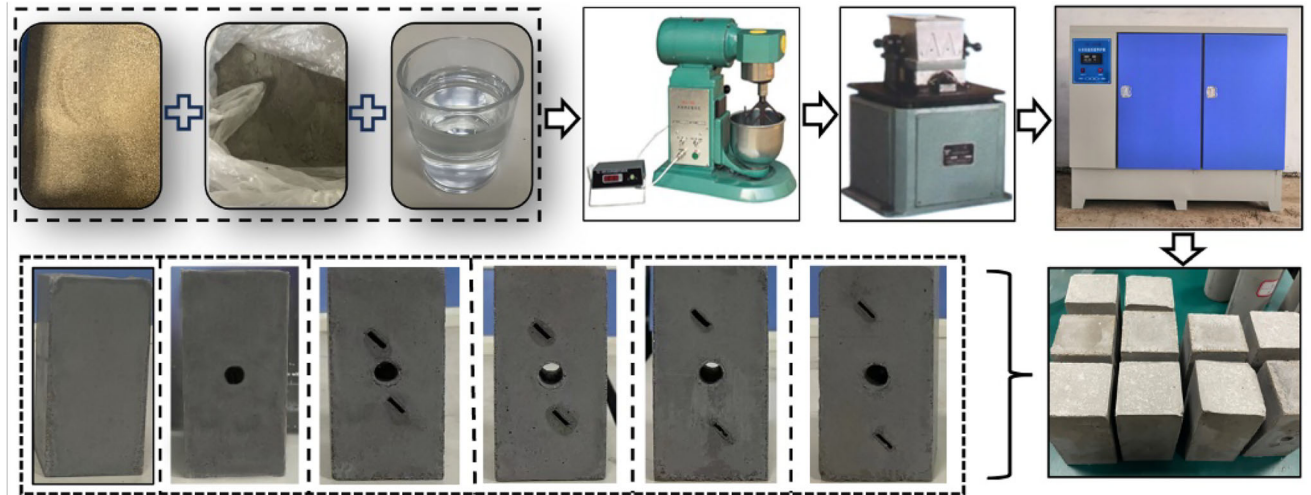
**Fig. 1** Mold picture and size



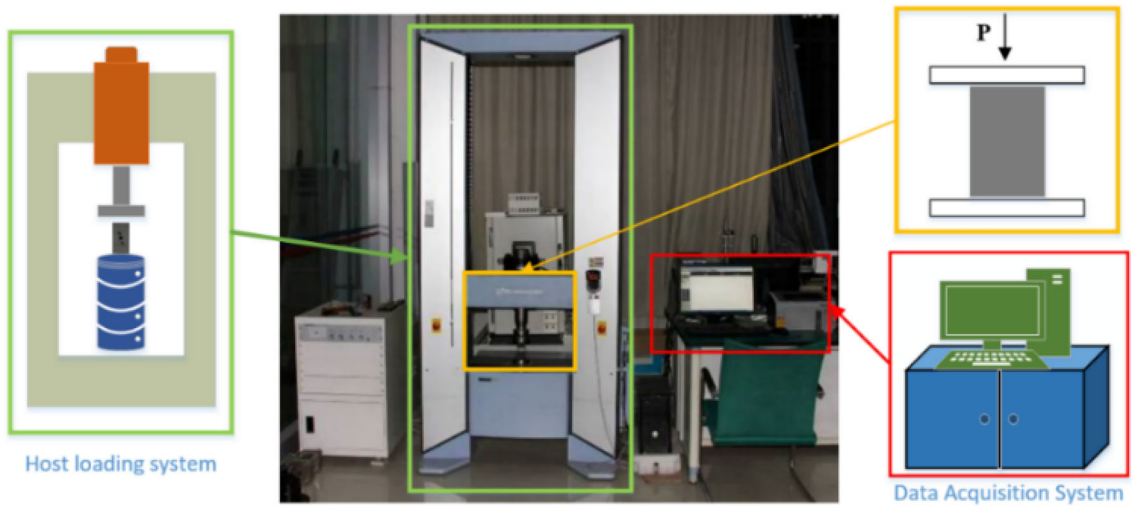**Fig. 2** Rock-like samples with single hole and double cracks
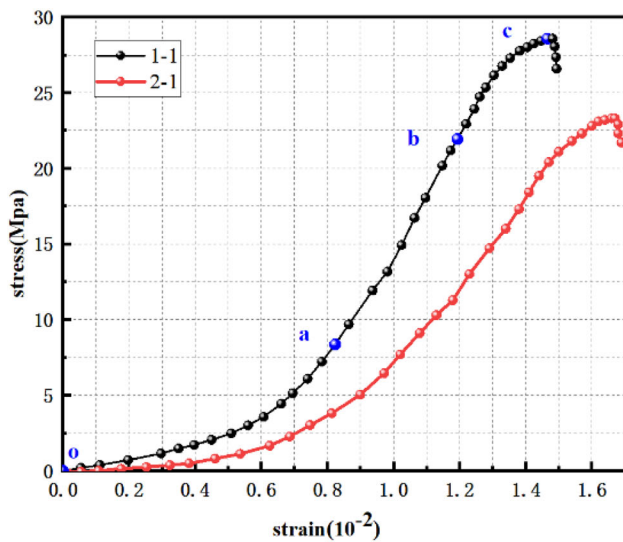


**Fig. 3** Uniaxial compression experimental equipment
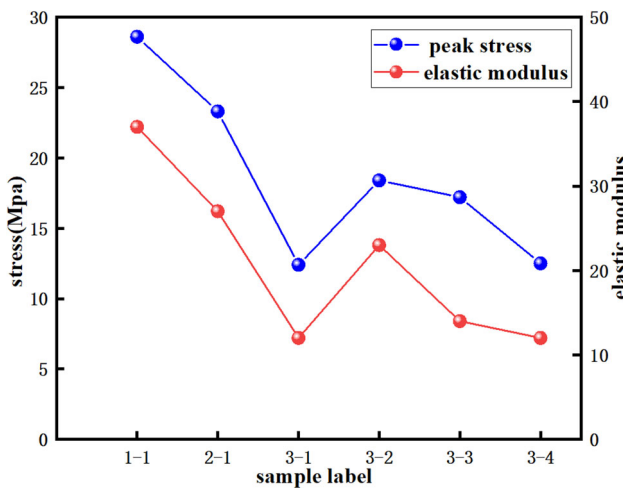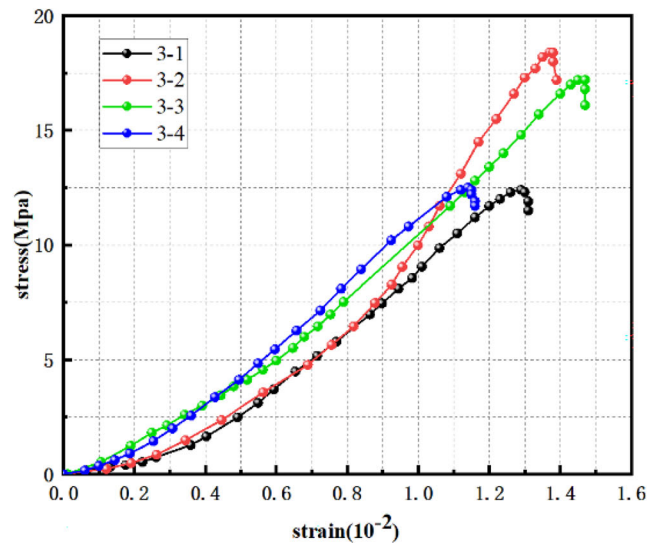
**Fig. 4** Stress–strain



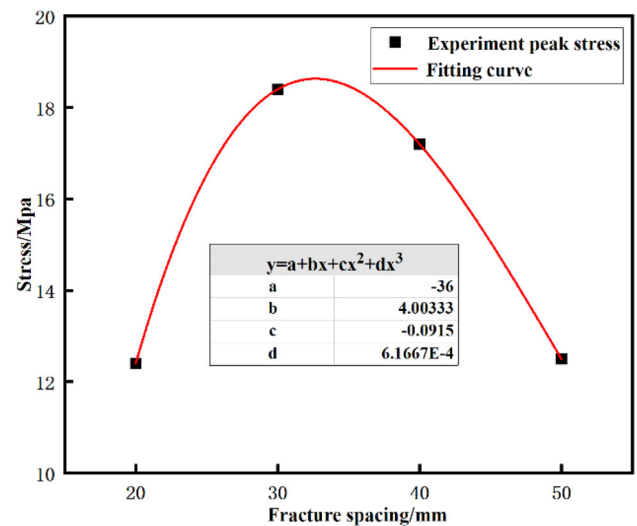**Fig. 5** Peak stress and elastic modulus of the sample



**Fig. 6** Comparison of experimental and simulation results

### 2.3.2 Failure mode analysis

The final failure modes of intact specimens, single hole specimens, and single hole double crack specimens under uniaxial compression are shown in Fig. 7. It can be seen from 1-1 that the intact rock sample consists of an inclined shear crack that runs through the top to the bottom of the sample. Secondary cracks sprout near the main crack at the top and bottom of the sample; 2-1 rock samples containing single hole, with cracks distributed on the upper and lower sides and left and right sides of the pores, mainly composed of macroscopic shear cracks, but there are also a small number of tensile cracks; 3-1 to 3-4 specimens with single hole and double cracks are mainly distributed between hole and cracks, as well as near the outer end of the cracks. When the crack spacing is 20 mm, there are shear cracks between the holes

and cracks, and tensile cracks are mainly found near the outer ends of the two cracks. As the crack spacing increases, tensile cracks gradually become the main cracks between the holes and cracks.

## 3 Numerical simulation analysis of damage and failure of rocks with voids and cracks

### 3.1 Numerical model establishment

PFC$^{3D}$, namely, three-dimensional particle flow program, is a method proposed by Peter Cundall and developed by
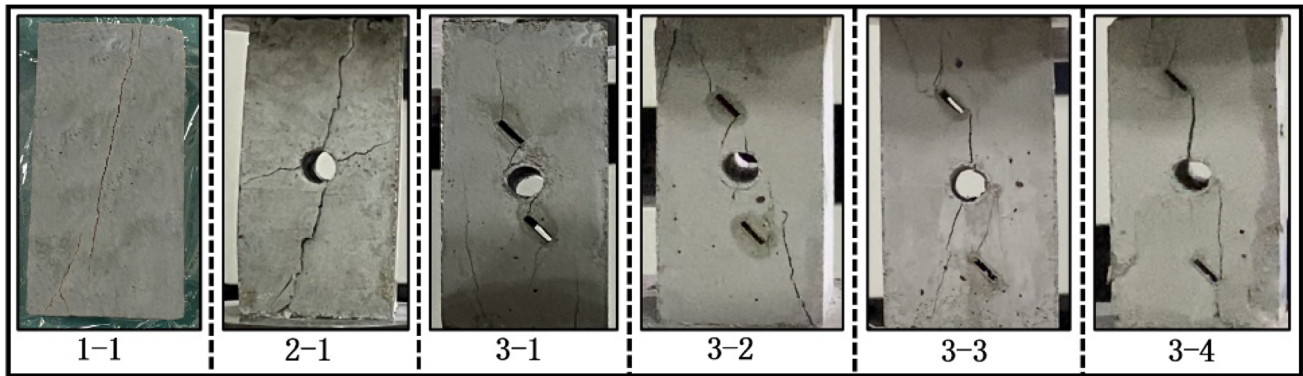
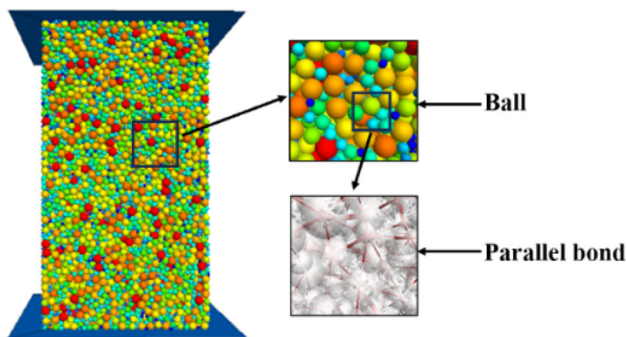**Fig. 7** Sample failure mode diagram



**Fig. 8** Schematic diagram of the complete numerical model

ITASCA in the US [24–26]. It mainly simulates the particles and the contact between particles in the model from the mesoscopic perspective. It is often used to simulate the mechanical properties of rocks. By preparing FISH language in PFC³ᴰ, rock samples with different working conditions can be restored. It can be used to study the interaction and movement between particles under different working conditions [27–35]. It has good effects and advantages in analyzing the meso-mechanical characteristics and stable deformation of the model.

PFC³ᴰ was used for numerical simulation of uniaxial compression, the numerical model of intact rock samples was established as shown in Fig. 8. The model size was 50 mm × 50 mm × 100 mm. The particle radius was between 0.5 and 1.5 mm to generate random particles. The different colors of particles in figure represent different radius.

By writing the FISH language, the holes and cracks at the same location as the experimental rock specimens were generated, as shown in Fig. 9. Figure 9a shows a rock sample model with a single hole, (b)–(e) shows models with crack spacing of 20, 30, 40, and 50 mm, respectively.

In the particle flow method, the mesoscopic parameters of a single particle are assigned to make materials with different properties reflect different constitutive properties in the simulation. When the mesoscopic parameters of each model

material and object are different, the macroscopic mechanical properties and constitutive relations reflected by the material and model in the simulation are also different [36]. For PFC, there are three types of contact constitutive models: stiffness model, sliding model, and bond model. The stiffness model specifies a certain elastic connection between contact force and relative displacement. The sliding model is a model established between normal and tangential forces regarding the mutual motion of two contact spheres. The bonding model limits the maximum combined force of normal and shear forces. Based on the characteristics of uniaxial compression, a bonding model is selected. And bonding models are also divided into two types: contact bond model and parallel bond model. The difference between these two models is that the contact area of the parallel bonding model is a block, while the contact area of the contact bonding model is a point. The parallel bonding model can simultaneously transmit force and torque, while the contact bonding model can only transmit force. According to the basic rock-like conditions to be simulated in the experiment, the parallel bond model is selected in this paper, which is regarded as a series of springs. These springs are uniformly distributed on the contact surface, centered on the contact point, and have constant normal and tangential stiffness [37]. Therefore, the relative motion at the contact point will generate force and bending moment, as shown in Fig. 10a. The mechanical behavior of a parallel-connected spring is similar to that of a beam with length L approaching O, as shown in Fig. 10b.

In this model, it is considered that the contact between two particles is generated within a certain range, and when two particles are in contact with each other, the model can transmit both the force and the moment, and the maximum normal stress acting on the adhesive material is as follows:

$$\tilde{\sigma} = \frac{T}{A} + \frac{|M|\overline{R}}{I} \tag{2}$$

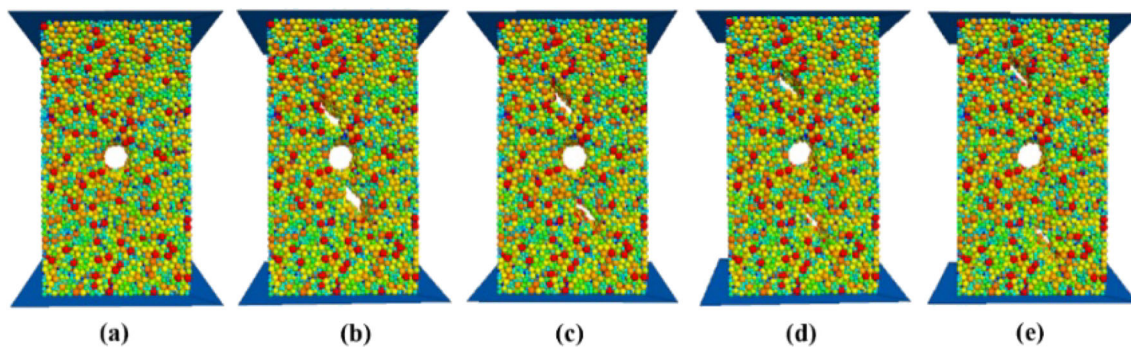The maximum tangential stress is as follows:

**Fig. 9** Schematic diagram of a complete model for numerical simulation

**Fig. 10** Parallel bond model and force diagram ($F_n$ for normal stress, $F_s$ for tangential stress, $K_n$ for normal stiffness, $K_s$ for tangential stiffness, $\overline{K_n}$ stiffness for the parallel method, $\overline{K_s}$ for parallel tangential stiffness, T as the axial force, V for tangential force, M for bending moment, and $M_t$ for torque)



(a) Schematic diagram of parallel bond model

(b) Force diagram of connection material of parallel connection model
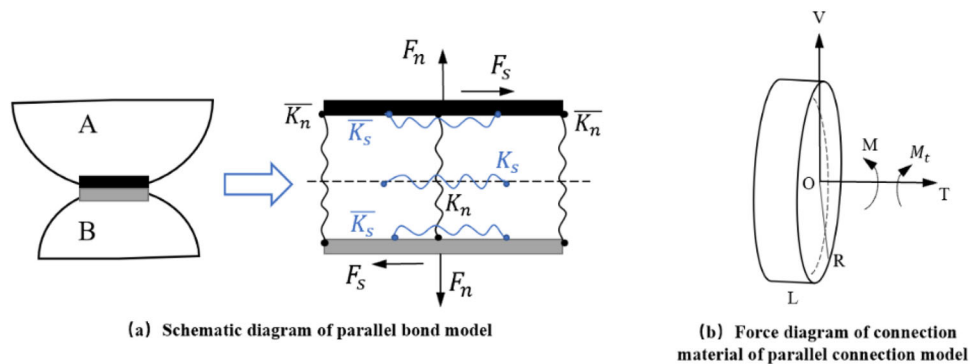
$$\overline{\tau} = \frac{|V|}{A} + \frac{|M_t|R}{J} \qquad (3)$$

where $A$, $I$, $J$, and $R$ are, respectively, the area, moment of inertia, stage moment of inertia, and parallel bond radius of the circular section of the parallel connection model. Once the shear or normal stress exceeds the strength limit, the particle constraint disappears.

## 3.2 Selection of microscopic parameters

PFC$^{3D}$ software represents the mechanical properties of objects by calibrating mesoscopic parameters, which cannot be directly obtained through laboratory tests. Therefore, before numerical simulation of uniaxial compression is carried out on the model, hypothesized mesomechanical parameters should be given to it [38]. Simulation tests should be carried out through the hypothesized parameters. After continuous selection and test calculation, the obtained macroscopic mechanical parameters are compared with the real indoor test. If the results are not satisfactory, the mesoscopic parameters need to be adjusted. Until the simulation results are basically consistent with the laboratory test results. It can be considered that this set of mesoscopic parameters can better simulate the rock-like failure mechanism. Based on the results of complete rock indoor experiments, this study
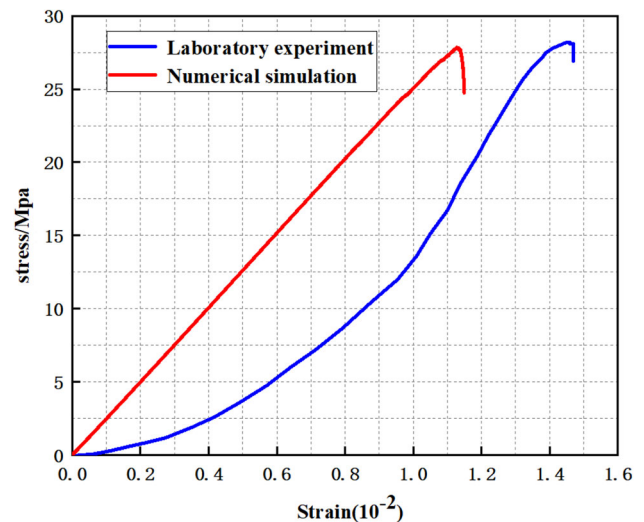


**Fig. 11** Comparison between experimental and simulation results of a complete rock model

adjusted the microscopic parameters in the PFC model using the "trial and error method" to obtain a numerical simulation stress–strain curve. Comparing the fitting of two curves from numerical experiments and indoor experiments, when the error between the mechanical parameters obtained from the two curves is small enough, it is considered that the fitting degree of the two curves is good, as shown in Fig. 11. The obtained rock microscopic parameters are the mechanical

**Table 1** Table of mesoscopic parameters for complete rock model

| Parameter | Emod/Gpa | kratio | fric | Pb_emod/Gpa | Pb_kratio | Pb_coh/Mpa | Pb_ten/Mpa | Pb_fa |
|---|---|---|---|---|---|---|---|---|
| Value | 1 | 1.5 | 0.3 | 3.2 | 1.5 | 32 | 13 | 10 |

*Emod* elastic modulus, *kratio* Poisson's ratio, *fric* friction coefficient, *Pb_emod* parallel bond modulus, *Pb_kratio* parallel bond stiffness ratio, *Pb_coh* parallel bond cohesion, *Pb_ten* parallel bond tensile strength, and *Pb_fa* parallel bonded internal friction angle

parameters required for numerical simulation. The simulated microscopic parameters are shown in Table 1.

The curve obtained from the experiment went through a compaction stage, an elastic deformation stage, and a stable development stage before reaching its peak. However, due to the influence of PFC loading mechanism, there is no compaction stage in the simulated curve [39]. This is because during the initial phase of particle formation, the sphere has been "compacted" under the effect of its gravitational acceleration to achieve self-balance, thus making the effective contact of the sphere reach the ideal state. In the test, there are microcracks in the rock-like specimen, so the curve shows nonlinear growth. The indirect contact of particles in PFC$^{3D}$ model is relatively uniform, and the simulated curve shows a linear growth.

### 3.3 Numerical result analysis

#### 3.3.1 Mechanical property analysis

In order to verify the rationality of the mesoscopic parameters selected in Sect. 3.2, this paper uses the mesoscopic parameters in Table 1 for uniaxial compression analog verification of the numerical model. The simulation adopts displacement loading method, and the upper loading plate is loaded downwards at a rate of 0.01 mm/s until the sample is damaged. Compare the peak intensity of the model obtained by the PFC program with the indoor test results, as shown in Fig. 12. From the figure, it can be seen that the peak stress of rocks with single hole is much higher than that of rocks with single hole and double cracks. The difference in peak strength between the experimental and simulated values is the largest, with a difference of 1.6 Mpa and a relative error of 6.4%. The difference between the experimental and simulation results of rock samples with single hole and double cracks under four types of crack spacing is very small, so this numerical simulation can basically reflect the indoor test results.

In PFC$^{3D}$, the interaction between particles is realized through contact. The contact energy between particles ultimately affects the macroscopic mechanical properties of the specimen. The contact force between particles is generated by squeezing and shearing between particles. It can quantitatively reflect the damage degree of rock-like samples under uniaxial compression. The distribution of contact force
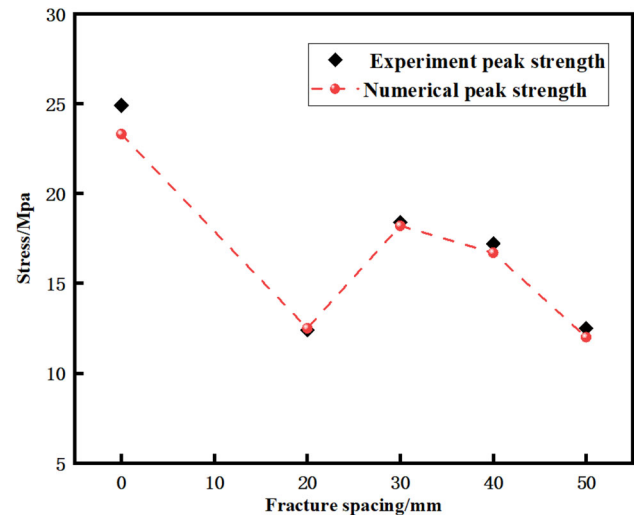


**Fig. 12** Comparison between indoor testing and simulated peak strength of rock-like materials

between particles is coupled with the development of microcracks. Many contact forces interleaved together form the contact force chain. The contact force chain can be used to characterize the nature (tension or compression), size, and direction of the contact force between particles. Therefore, we analyze the contact force between particles of prefabricated rock specimens with holes and cracks at different strain stages. The contact force chain at different stages of the five samples is shown in Fig. 13. In the figure, (a) is the contact force chain diagram of the rock sample model with single hole, and (b)–(e) is the contact force chain diagram of the rock sample model with single hole and double cracks with crack spacing of 20, 30, 40, and 50 mm, respectively. I–IV represents 30% and 70% of the peak stress before the peak, the peak point, and 70% of the peak stress after the peak. In the figure, the green contact force chain indicates that the contact force is tension, and the blue contact force chain indicates that the contact force is pressure. In the figure, the thickness of the contact force chain corresponds to the size of the contact force. The thicker the force chain, the greater the contact force. The direction of the force chain represents the direction of the contact force.

According to Fig. 13, it can be observed that during the entire loading process, for the single hole model, there is a concentrated distribution area of green force chains on the

**Fig. 13** Contact force chain diagram
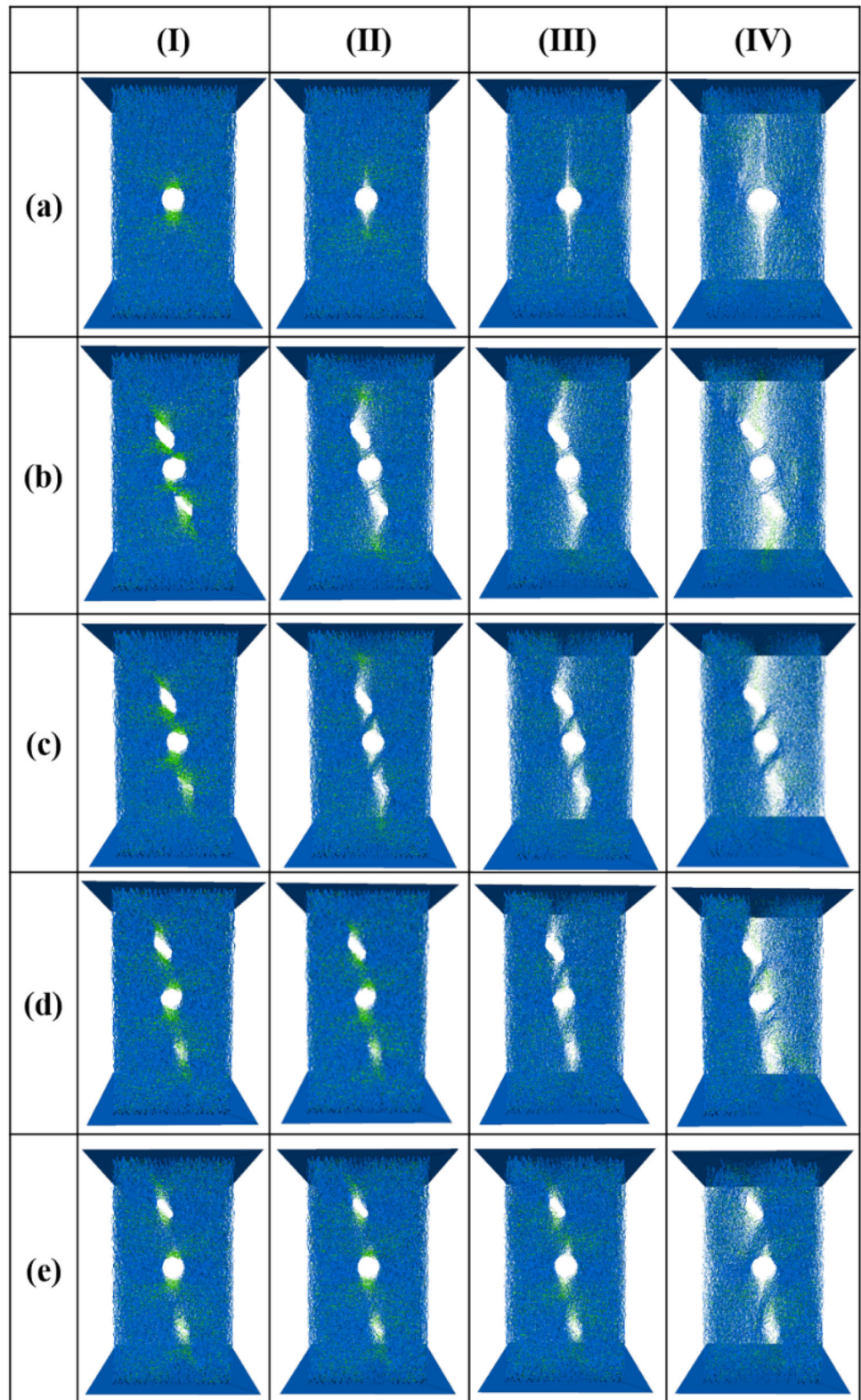
upper and lower sides of the hole, indicating that the position is heavily tensioned. The force chain on the left and right sides of the hole is thicker, and the contact force is larger. With the progress of loading, due to the phenomenon of stress concentration, the contact bond between particles at the vertical direction of the hole center breaks, and the contact force disappears. For the single hole and double cracks model, the force chain between the two cracks and the hole and near the outer tip of the crack is almost all green. It shows that there is an obvious tension area at this position, and the rest of the force chain is mainly under pressure. The force chain at the horizontal plane formed when the outer tips of the two cracks extend to the sides close to each other is thicker. It shows that the contact force at the horizontal plane is larger. Moreover, with the increase in the gap between cracks, the contact force in the horizontal direction where the holes are located also increases gradually. This is because the particles basically move in the vertical direction, and the displacement direction is perpendicular to the horizontal direction. The friction caused by the dislocation of particles increases the contact force. With the progress of loading, the relative displacement between particles increases, and the contact force between particles gradually disappears. Moreover, due to the phenomenon of stress concentration, the contact bond between particles breaks, and the bonding force also gradually drops to zero. Therefore, the contact force chain gradually disappears in the vertical direction of the crack and the hole. On the whole, the contact force chain can be used to analyze the force and stress–strain mechanism generated by the mutual sliding and contact between particles.

### 3.3.2 Analysis of acoustic emission characteristics

In the process of stress, cracks will occur inside the rock and continue to expand and extend. The cracks will be released in the form of elastic waves, resulting in acoustic emission phenomenon. Therefore, acoustic emission can be used to monitor the deformation and failure process of the sample. The failure of the sample is a gradual process and does not occur suddenly. When the sample is loaded, internal damage occurs. Each occurrence of an acoustic emission event corresponds to the formation of a microcrack inside the rock.

The stress–strain-acoustic emission event curve relationship of different model specimens is shown in Fig. 14. From the figure, it can be seen that the stress curve of the model specimen during uniaxial loading corresponds to the acoustic emission characteristics. In the early stage of loading, there was almost no acoustic emission phenomenon. Because the stress borne by the particles in the model did not exceed their bonding strength, and the model was still in a basically stable state. As the loading progresses, acoustic emission phenomena begin to occur, but the number of acoustic emission events remains basically stable. When loaded to the

peak stress, the number of acoustic emission events rapidly increases, indicating that the sample undergoes significant damage during this stage.
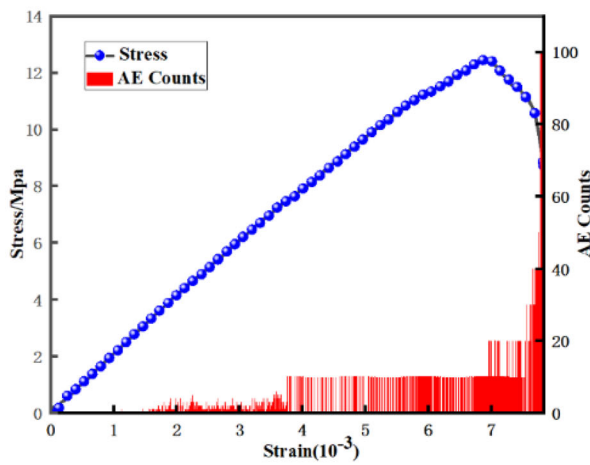
### 3.3.3 Particle displacement analysis

The movement of meso-particles in rock determines the macroscopic deformation of rock under stress. Analyzing the displacement characteristics of meso-particles is helpful to explain the deformation and failure mechanism of rock. In PFC$^{3D}$, it is very convenient to observe the displacement of microscopic particles in the model. Figure 15 shows the particle displacement cloud map of different model samples during the loading process. In the figure, (a) shows the particle displacement map of the rock sample model with a single hole, and (b)–(e) represents the particle displacement map of the rock sample model with a single hole and a double crack spacing of 20, 30, 40, and 50 mm, respectively. I-IV represents the peak stress before peak at 30%, 70% and peak point, as well as 70% post-peak stress. Five sets of models are set with the same displacement interval, and the particle color ranges from blue to red to indicate the displacement from small to large.

By observing the color of the particles, it can be seen that for the single hole model, the particle displacement in the early stage of loading is basically a horizontal layered distribution. The particle movement at the upper loading plate is more active than that at the lower part. As the loading reaches its peak, the particle displacement is bounded by the centerline, with the upper particles exhibiting a positive V-shaped distribution and the lower particles exhibiting an inverted V-shaped distribution. For the single hole and double cracks model, in the early stage of loading, the particle displacement can be roughly seen as a horizontal layered distribution. As the loading progresses, the particle displacement follows the inclined direction of the crack, with the upper particles showing a positive V-shaped distribution and the lower particles showing an inverted V-shaped distribution. The particle displacement of the model with crack spacing of 30 and 40 mm is larger than that of the other two. After the peak, with the occurrence of local damage and small cracks, the particle displacement in the upper area of the connection direction between the two cracks and the hole is the largest. The particle displacement shows an irregular distribution, resulting in displacement dislocation and the formation of oblique shear bands in the areas with more active crack development. Comparing the particle displacement distribution of five model samples, the fracture situation of each sample during loading can be obtained. Through analysis, it can be concluded that the failure situation of the sample is basically consistent with the indoor test.
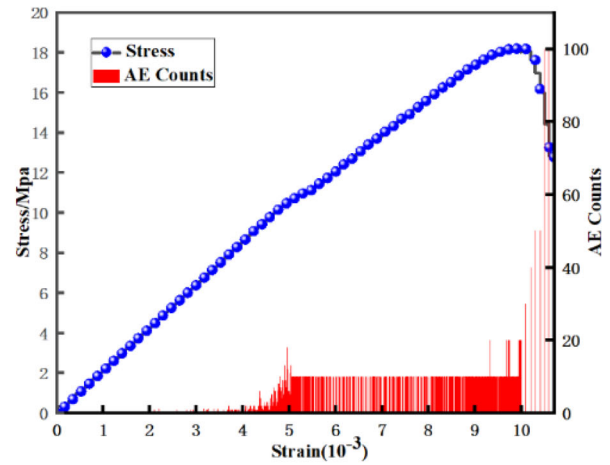
Further analyze the influence of crack spacing on the particle displacement of the sample model. Analyze the particle
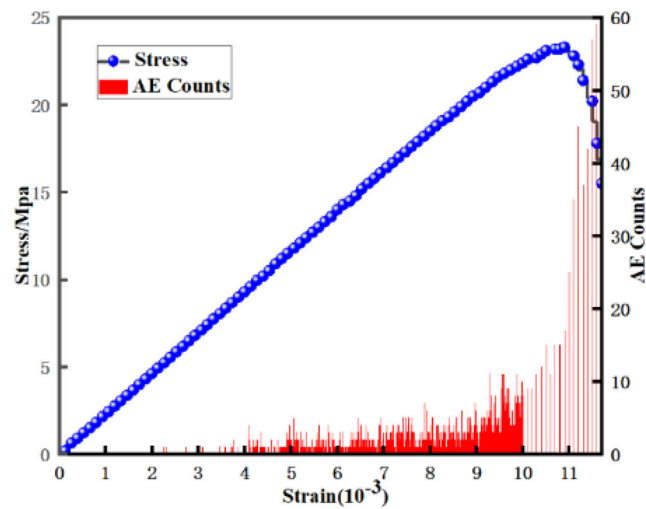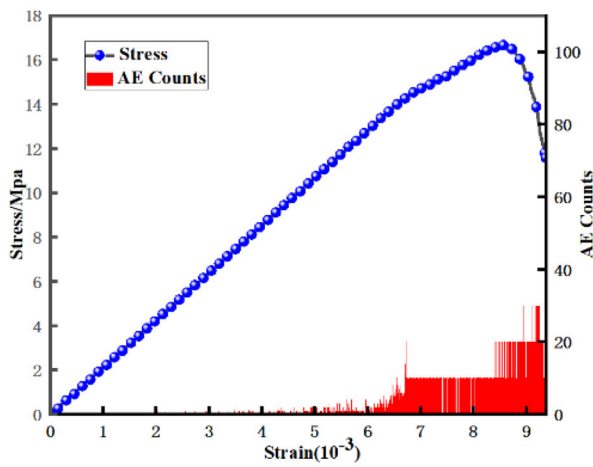
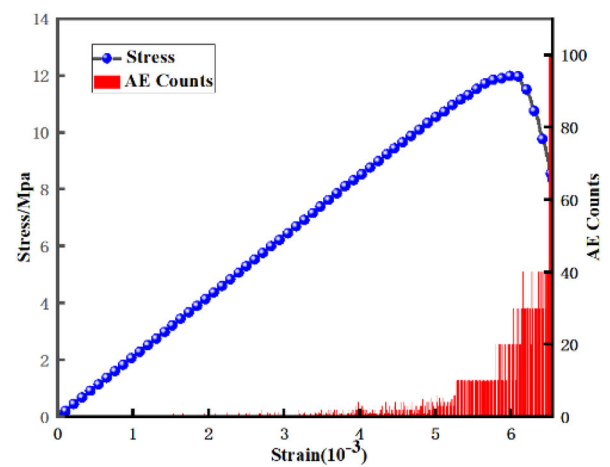**(a) rock like sample model with single hole**



**(b) crack spacing 20 mm**



**(c) crack spacing 30 mm**



**(d) crack spacing 40 mm**



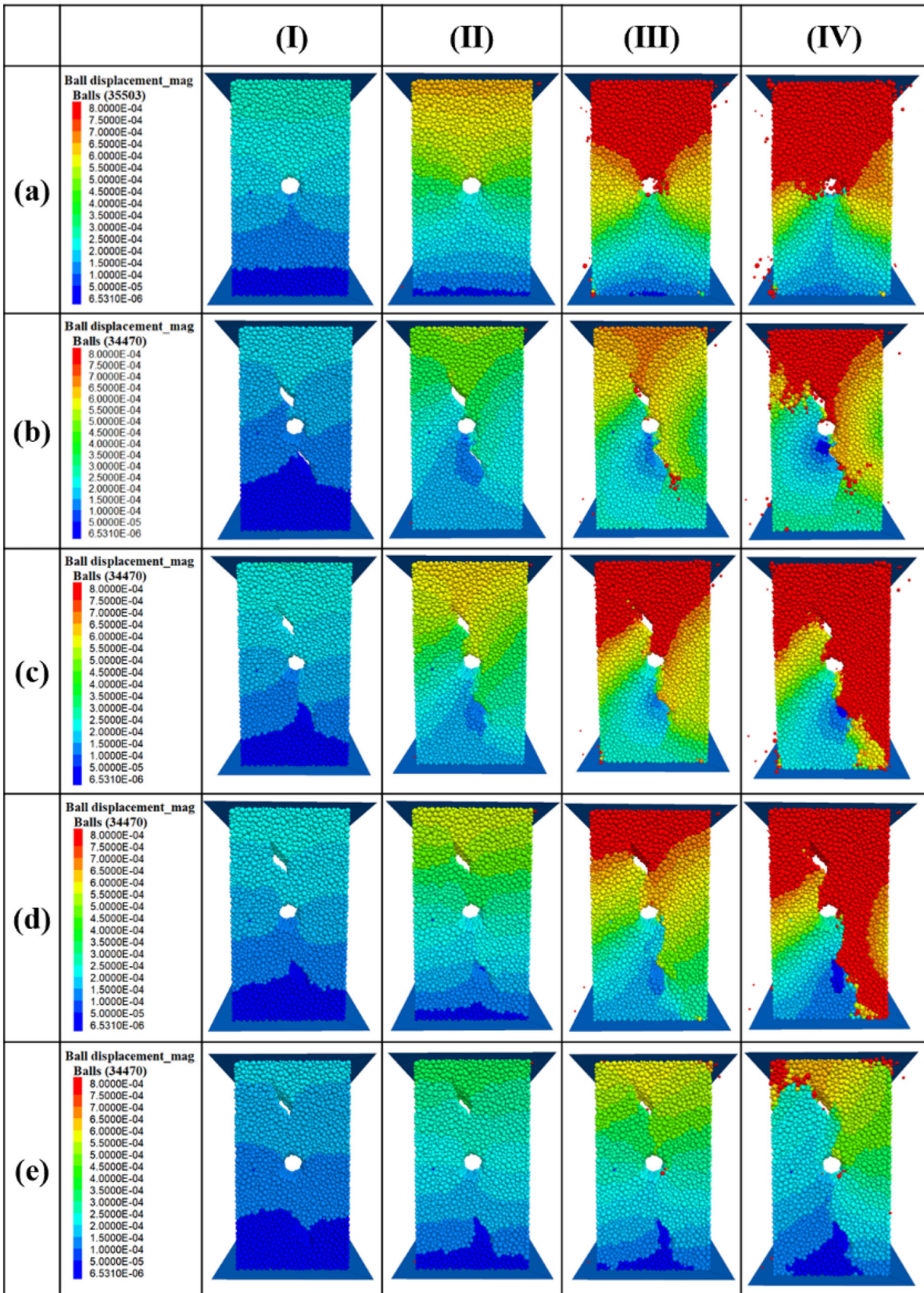**(e) crack spacing 50 mm**

**Fig. 14** Stress–strain-acoustic emission events
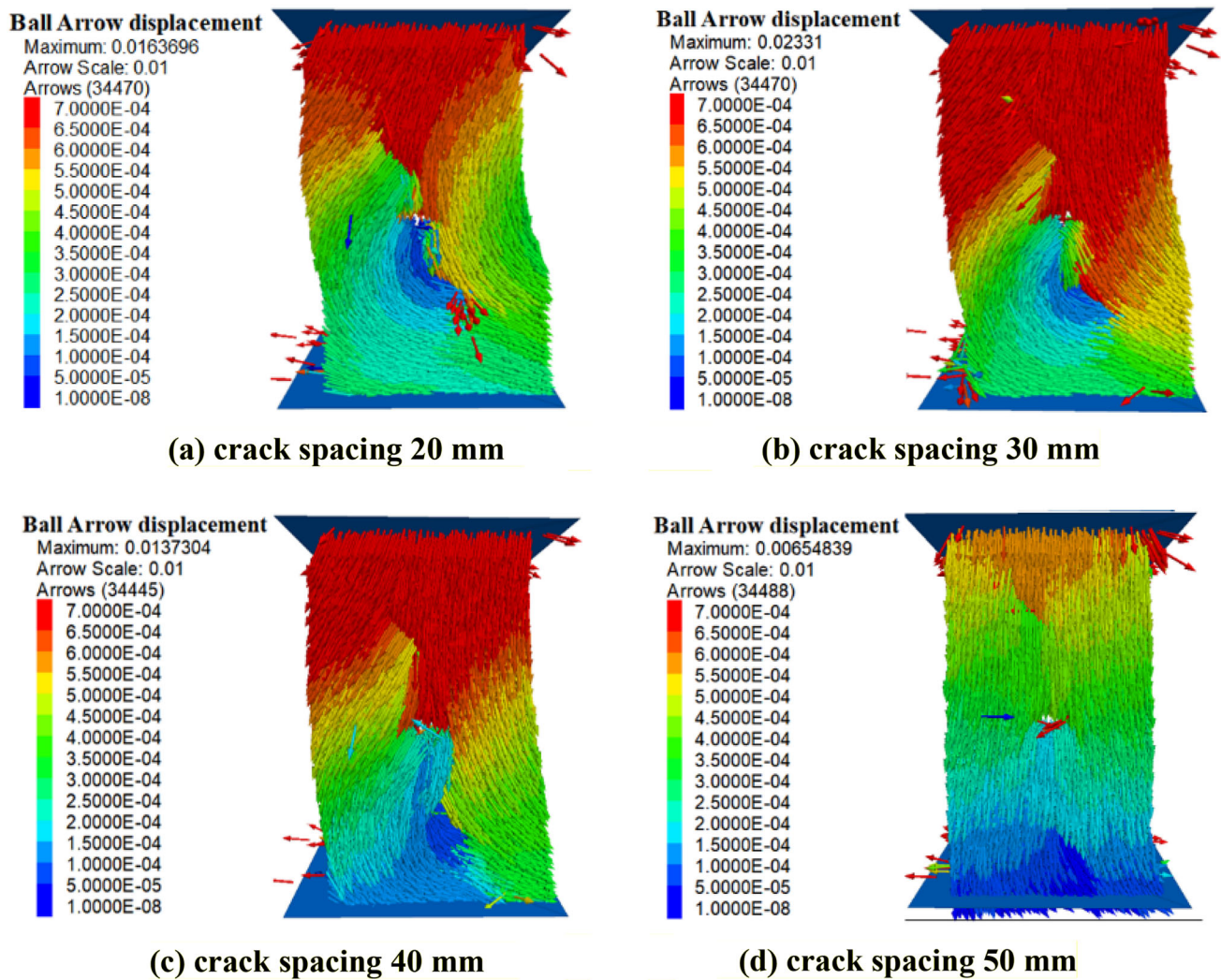
**Fig. 15** Particle displacement diagram

**(a) crack spacing 20 mm**

**(b) crack spacing 30 mm**

**(c) crack spacing 40 mm**

**(d) crack spacing 50 mm**

**Fig. 16** Grain arrow displacement diagram

displacement vector map of the model sample at the peak point under four different crack spacing conditions, as shown in Fig. 16. The color of the arrow in the figure represents the displacement magnitude, and the direction of the arrow is the direction of particle movement relative to the initial position. Due to the downward movement of the upper loading plate during the model loading process, the direction of particle movement can be roughly seen as going counterclockwise. From Figure (b), it can be seen that when the distance between the two cracks is 30 mm. The maximum particle displacement is about 23.3 mm. Shear failure occurs in the middle of the sample, forming a shear failure surface along the direction of the connecting line between the two cracks. When the distance between two cracks in Figure (d) is 50 mm, the maximum particle displacement is the smallest, only 6.5 mm, and the particle displacement distribution is relatively uniform.

### 3.3.4 Failure mode analysis

The evolution of microcrack growth contains abundant information. The analysis of the crack evolution characteristics of the sample can not only increase the understanding of the mechanical behavior of the sample, but also clarify the evolution of the sample during the failure process. In PFC$^{3D}$, the contact force among particles in the model changes during the application of loads. When the contact force undergoes tensile stress and exceeds the normal bond strength, the contact force breaks and generates tensile cracks. When the contact force undergoes shear stress and exceeds the tangential bond strength, the contact force breaks and generates shear cracks. All the tensed-shear microcracks join together to form macroscopic cracks on the specimen surface. In this section, the number of microcracks, the number of tensile shear cracks, and the evolution process of crack growth were studied.
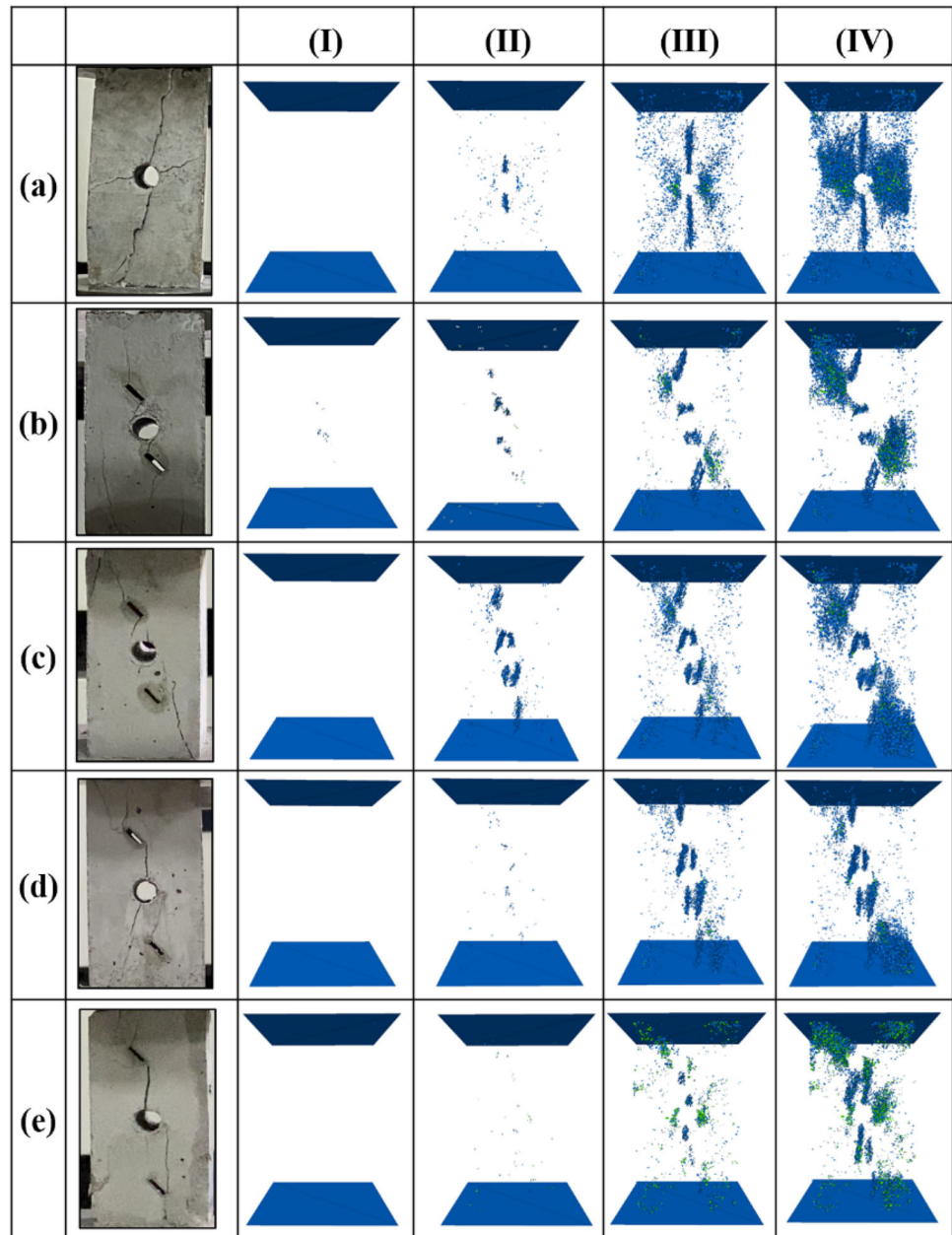
**Fig. 17** Crack initiation and propagation diagram



Figure 17 shows the initiation and propagation process of microcracks in the specimen during uniaxial loading, with green indicating shear cracks and blue indicating tensile cracks. In the figure, (a) is the expander graph of the rock sample model with single hole, (b)–(e) is the expander graph of the rock sample model with single hole and double cracks with crack spacing of 20, 30, 40, and 50 mm, respectively. I–IV represents 30%, 70%, and 70% of the peak stress before the peak, and 70% of the peak stress after the peak, respectively.

It can be seen that the final failure situation of the simulated model sample is basically consistent with the indoor test. For the single hole model, microcracks first appear at

the upper and lower ends of the hole, and gradually propagate upwards and downwards. As the loading progresses, a large number of microcracks appear on the left and right sides of the hole. For the single hole double cracks model, it can be seen that during the crack initiation stage, when the crack spacing is 20 mm, microcracks appear between the inner end of the two cracks and the hole. As the crack spacing increases, cracks are initiated near the outer tip of the crack, and microcracks between the inner end of the crack and the hole decrease. At the peak stress, microcracks near the outer tips of the two cracks exhibit an upward and downward propagation trend. As the crack spacing increases, microcracks
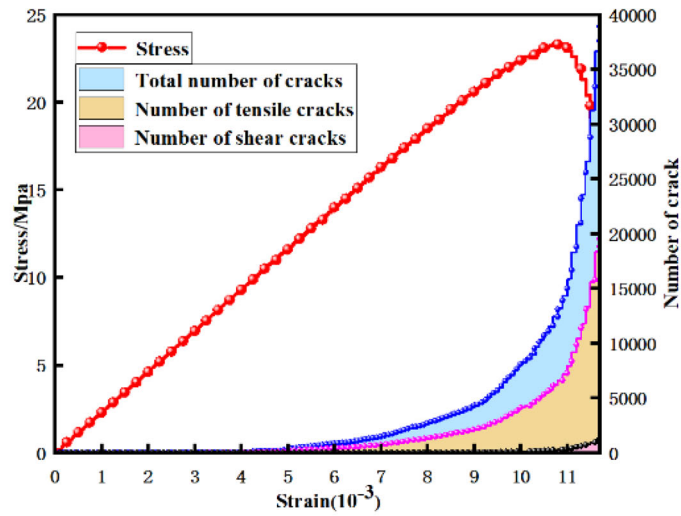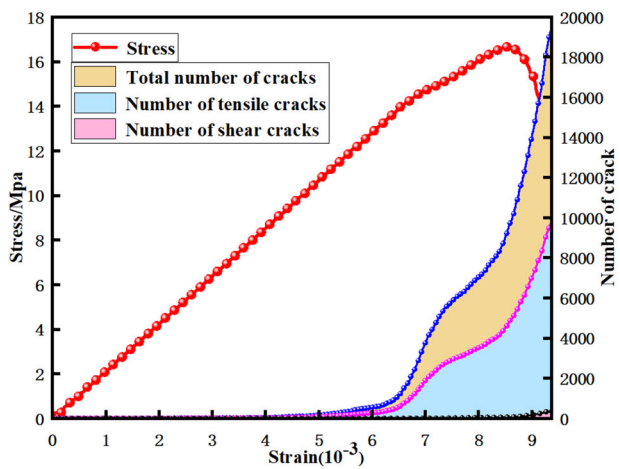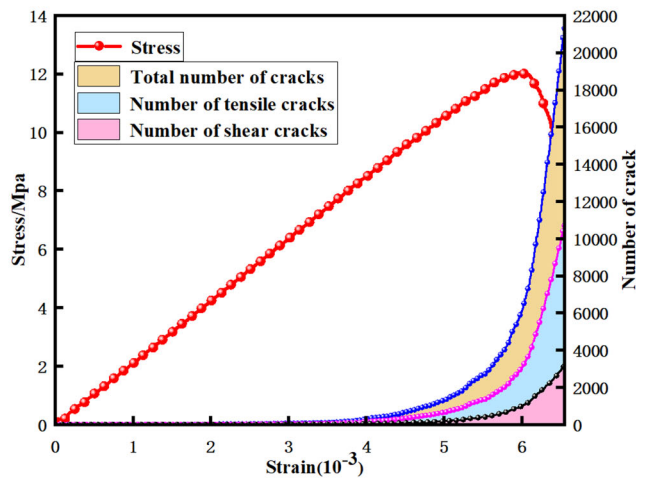
**(a) rock like sample model with single hole**
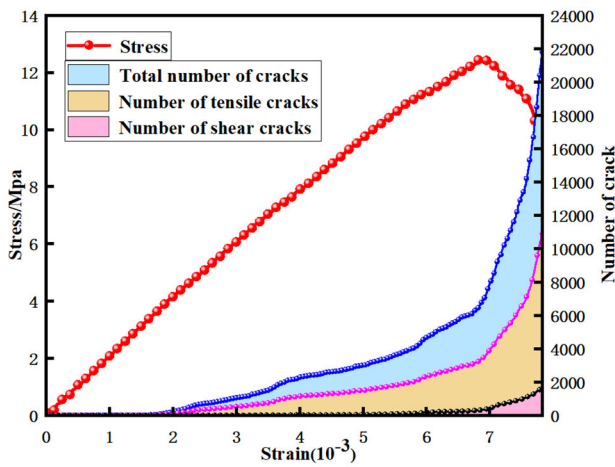


**(b) crack spacing 20 mm**
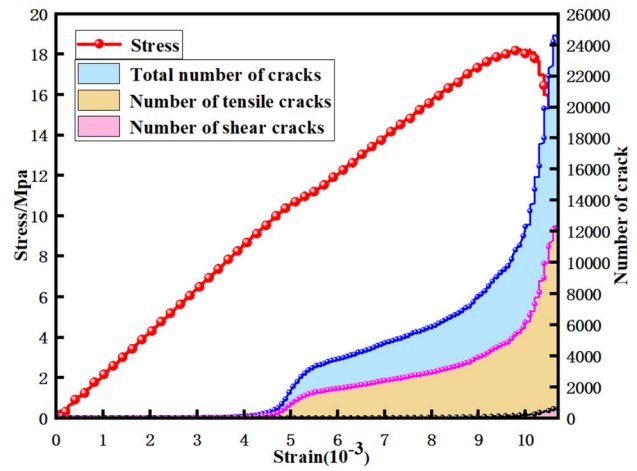


**(c) crack spacing 30 mm**



**(d) crack spacing 40 mm**



**(e) crack spacing 50 mm**

**Fig. 18** Microcrack number evolution diagram

between the inner ends of the two cracks and the holes gradually distribute vertically along the horizontal diameter of the holes. After the peak, a large number of microcracks continue to propagate at the same location as the peak.

In the loading process of rock-like samples, microcracks tend to appear at the most vulnerable part of the sample. According to the analysis, when the crack spacing is 20 mm, the middle of the two cracks and the hole is the vulnerable area. With the increase in the crack spacing, the distance between the outer end of the crack and the top and bottom of the sample is shortened, and the area near the inner and outer tips of the two cracks gradually becomes the vulnerable area.

Figure 18 shows the variation of the total number of microcracks and the number of tensile and shear cracks with increasing strain in the model sample during servo loading. Overall, the microcracks generated by the rock-like model specimens under loading are mainly tensile cracks. And the number of cracks increases sharply near the peak stress. When the crack spacing in Figure (b) is 20 mm, microcracks initiate earliest, with a peak number of 3620 microcracks, including 3247 tensile cracks and 373 shear cracks. When the crack spacing in Figure (c) is 30 mm, the number of microcracks at the peak is the highest, about 5350. The microcrack initiation is the latest under this crack spacing, indicating that the model is the least prone to failure under this crack spacing. When the crack spacing in Figure (d) is 40 mm, the proportion of tensile cracks is the highest, and at the peak, the number of tensile cracks accounts for about 98% of the total number of cracks. When the crack spacing in Figure (e) is 50 mm, the number of microcracks is the lowest, but the number of shear cracks is higher than that under the other three cracks spacing. The number of shear cracks at the peak is 917, accounting for approximately 33% of the total number of cracks.

### 3.3.5 Failure mechanism analysis

It can be seen that for the single hole model, cracks are mainly concentrated in the upper and lower parts of the hole. This is due to the presence of stress concentration at this location. The mechanical analysis model of the single hole model is shown in Fig. 19. According to the theory of linear elasticity, the stress distribution of rock mass under the influence of circular holes is as follows:

$$\left.\begin{array}{l} \sigma_\rho = \frac{P}{2}\left[\left(1 - \frac{R_a}{\rho}\right) - \left(1 - 4\frac{R_a^2}{\rho^2} + 3\frac{R_a^4}{\rho^4}\right)\cos2\theta\right] \\ \sigma_\theta = \frac{P}{2}\left[\left(1 + \frac{R_a}{\rho}\right) + \left(1 + 3\frac{R_a^4}{\rho^4}\right)\cos2\theta\right] \\ \tau_{\rho\theta} = -\frac{P}{2}\left[\left(1 + 2\frac{R_a^2}{\rho^2} - 3\frac{R_a^4}{\rho^4}\right)\sin2\theta\right] \end{array}\right\} \quad (4)$$

wherein $\sigma_\rho$, $\sigma_\theta$, and $\tau_{\rho\theta}$ are the radial stress, tangential stress, and shear stress in the polar coordinate system, and $(\rho, \theta)$ are the polar coordinates of the points around the hole. When
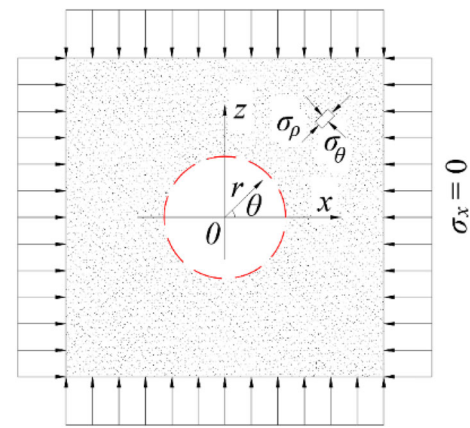


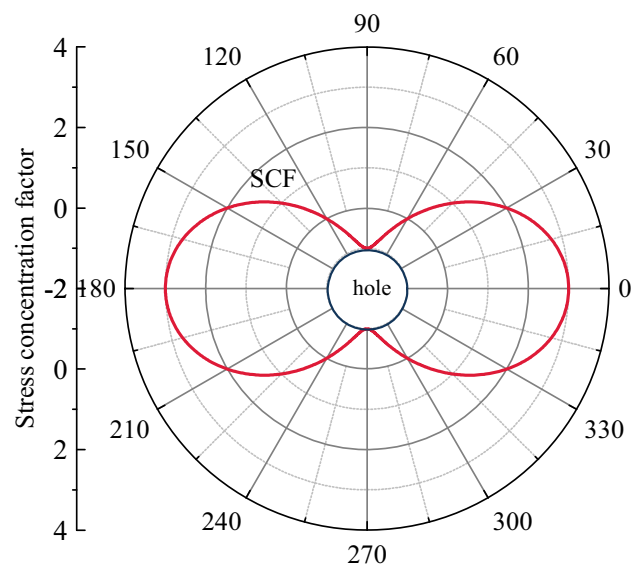**Fig. 19** Mechanical analysis model of single hole model



**Fig. 20** Stress concentration factor (SCF) of single hole model

$\rho = R_a$, Eq. (4) can be simplified as follows,

$$\left.\begin{array}{l} \sigma_\rho = 0 \\ \sigma_\theta = P[1 + 2\cos2\theta] \\ \tau_{\rho\theta} = 0 \end{array}\right\} \quad (5)$$

Figure 20 shows the stress concentration factor (SCF) of a single hole. From the figure, it can be seen that under uniaxial compression, the stress concentration on the defect hole side can reach 3, while the stress concentration in the upper and lower parts is negative, indicating that the upper and lower parts of the hole are subjected to tensile stress. Due to the concentration of tensile stress, the crack propagation of the defect hole extends from the upper and lower parts of the hole.

For the single hole double cracks model, due to the much lower stiffness of the crack surface than the non-crack surface, stress concentration occurs at the crack tip. When loaded to the crack initiation stress, microcracks will propagate along the crack tip and extend in the direction of the main stress. According to the theory of fracture mechanics, under the action of external load, a composite crack will be generated. According to the composite fracture criterion, the stress field at the crack tip can be obtained:

$$\begin{cases} \sigma_{r(\mathrm{I+II})} = \sigma_{r\mathrm{I}} + \sigma_{r\mathrm{II}} = \frac{1}{2\sqrt{2\pi r}}\left[K_{\mathrm{I}}(3-\cos\theta)\cos\frac{\theta}{2} + K_{\mathrm{II}}(3\cos\theta-1)\sin\frac{\theta}{2}\right] \\ \sigma_{\theta(\mathrm{I+II})} = \sigma_{\theta\mathrm{I}} + \sigma_{\theta\mathrm{II}} = \frac{1}{2\sqrt{2\pi r}}\cos\frac{\theta}{2}[K_{\mathrm{I}}(1+\cos\theta) - 3K_{\mathrm{II}}\sin\theta] \\ \tau_{r\theta(\mathrm{I+II})} = \tau_{r\theta\mathrm{I}} + \tau_{r\theta\mathrm{II}} = \frac{1}{2\sqrt{2\pi r}}\cos\frac{\theta}{2}[K_{\mathrm{I}}\sin\theta + K_{\mathrm{II}}(3\cos\theta-1)] \end{cases}$$

$$(6)$$

Among them, $\theta$ is the angle between microcracks and cracks; $r$ is the distance from the crack tip; $K_I$, $K_{\mathrm{II}}$ is the stress intensity factor of type I and II cracks.

Under uniaxial compression loading, when the crack length is L and the dip angle is $\beta$, the stress intensity factor is as follows:

$$\begin{cases} K_I = \sigma\sqrt{\pi L}\cos^2\beta \\ K_{\mathrm{II}} = \sigma\sqrt{\pi L}\sin\beta\cos\beta \end{cases} \tag{7}$$

The criterion for crack initiation under uniaxial compression conditions is as follows:

$$\begin{cases} \frac{\partial\sigma_\theta}{\partial\theta} = 0 \\ \frac{\partial^2\sigma_\theta}{\partial\theta^2} < 0 \end{cases} \tag{8}$$

Substituting Eq. (6) into Eq. (8) yields:

$$K_I\sin\theta + K_{\mathrm{II}}(3\cos\theta - 1) = 0 \tag{9}$$

Substituting Eq. (7) into Eq. (9) yields:

$$\tan\left(90^\circ - \beta\right) = \frac{1 - 3\cos\theta}{\sin\theta} \tag{10}$$

Because the inclination angle of the crack is 45°, it can be obtained that $\theta$ is about 53°, and the experimental and theoretical results are basically consistent.

# 4 Analysis of damage evolution characteristics of rocks with voids and cracks

## 4.1 Damage variables based on fracture mechanism

From the microscopic point of view, there are a lot of primitive microdefects in rock materials. Under the action of load and other factors, the appearance and expansion of microdefects in materials and the deterioration of macroscopic mechanical properties is called damage. In many geotechnical engineering researches, the damage variable is defined by the number of crack growth as the main variable. The evolution of the damage variable can reflect the change of the internal fine structure and macroscopic mechanical behavior of the material. The damage variable can be expressed in many forms, such as crack density, acoustic emission event number, pore area, etc. Based on the fracture mechanism of mesoscopic particles in $PFC^{3D}$, the mesoscopic damage variable is defined as the ratio of the number of intergranular fractures to the total number of intergranular bonds:

$$D = \frac{N}{N_0} \tag{10}$$

In the formula, N is the number of cracks of bonding between particles, namely, the number of cracks; $N_0$ is the total number of bonding between model particles.

## 4.2 Evolution characteristics of rock-like damage

Figure 21 shows the variation curves of stress and damage variables with strain for five simulated specimens with voids and cracks. According to the curves, the damage evolution process of model specimens can be divided into three stages: I is the non-damaging stage. In this stage, due to the initial loading, the contact force between particles in the model has little change, and the stress under the model has not exceeded the bonding strength. Therefore, the damage variable D is 0, and no crack is generated. II is the stable growth stage of damage. In this stage, the bond between some particles is destroyed. The microcracks begin to initiation gradually, but the damage develops slowly. It can be seen that the microcracks appear first in the model sample with the crack spacing of 20 mm, followed by the model sample with the crack spacing of 50 mm, and the microcracks appear late in the model sample with the crack spacing of 30 mm. III is the damage and destruction stage. At this stage, the damage variable first presents an almost vertical trend and increases rapidly. The stress decreases rapidly, and a large number of microcracks appear. When the damage variable increases to a certain value, it tends to be gentle. The model sample is in the residual deformation stage.
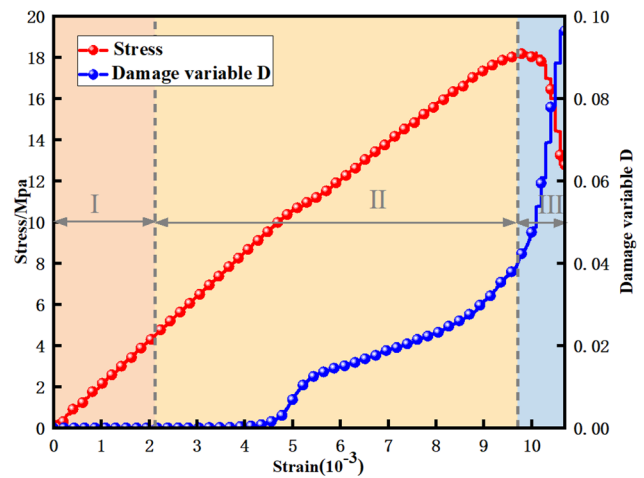
# 5 Conclusion

In this paper, through indoor uniaxial compression experiments and $PFC^{3D}$ grain flow numerical simulation, the
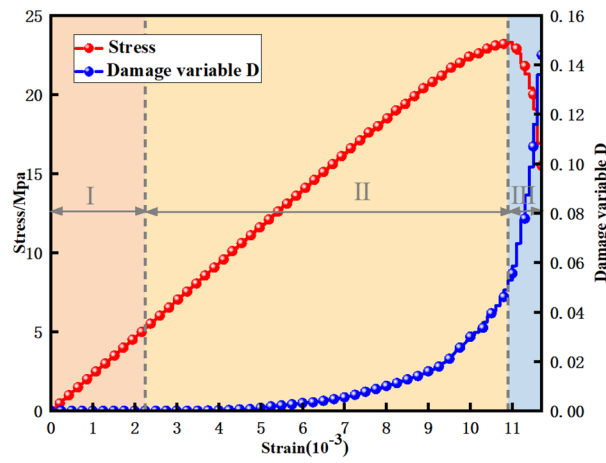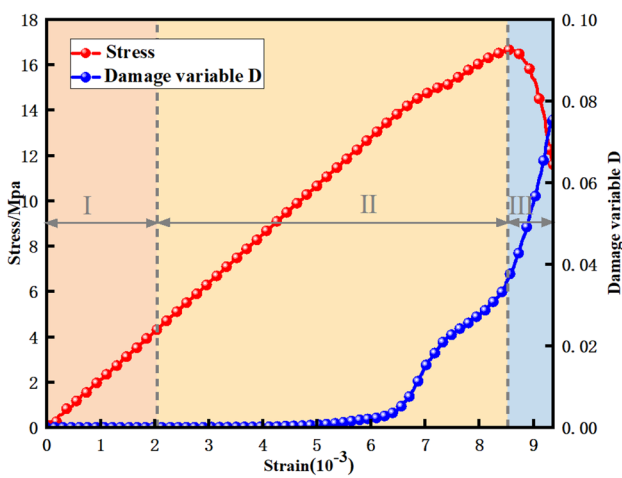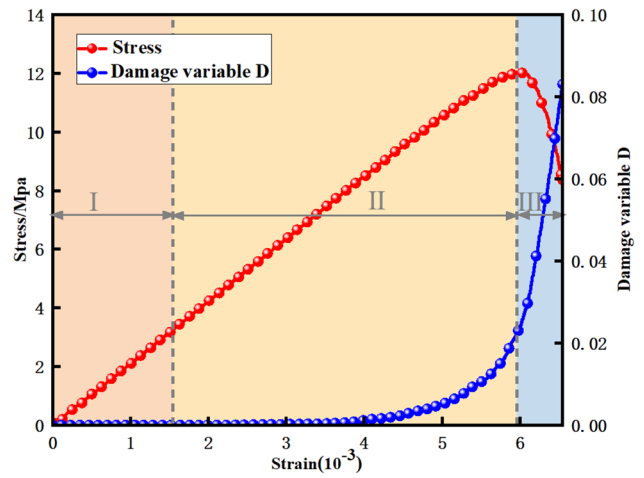
(a) rock like sample model with single hole
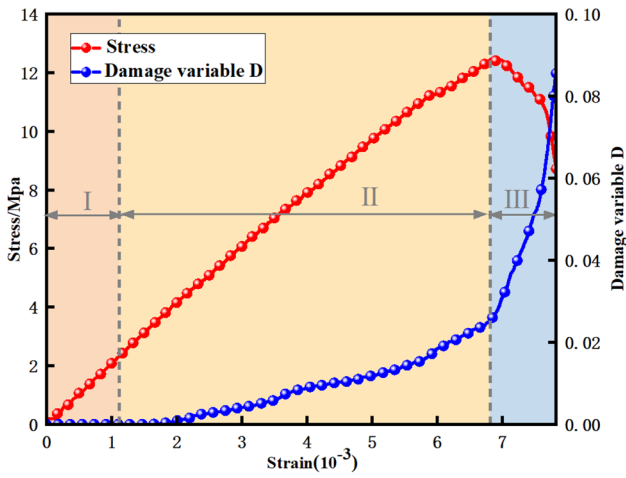


(b) crack spacing 20 mm



(c) crack spacing 30 mm



(d) crack spacing 40 mm



(e) crack spacing 50 mm

**Fig. 21** Stress–strain-damage variable

mechanical characteristics, acoustic emission properties, particle displacement, and failure modes of rock-like samples with holes and cracks at different locations are analyzed and studied. The following conclusions are drawn:

(1) The presence of holes and cracks can reduce the uniaxial compressive strength and elastic modulus of the sample. The yield point shows a trend of first increasing and then decreasing with the increase in crack spacing.

(2) During the entire loading process, the single hole model experiences severe tension on the upper and lower sides of the hole, resulting in high contact forces. The single hole double cracks model is a tensile zone between the two cracks and the hole, as well as near the outer tip of the crack, while the rest is heavily compressed. As the spacing between cracks increases, the contact force in the horizontal direction where the holes are located gradually increases. The acoustic emission event of the sample can be divided into three stages: silent emission stage, stable stage, and rapid growth stage.

(3) In the early stage of loading, the particle displacement basically exhibits a horizontal layered distribution. At the peak, the particle displacement is bounded by the centerline, with the upper particles exhibiting a positive V-shaped distribution and the lower particles exhibiting an inverted V-shaped distribution. For the single hole and double cracks model, the maximum particle displacement shows a trend of first increasing and then decreasing with the increase in crack spacing.

(4) There is a phenomenon of stress concentration on both sides of the hole and the crack tip, which can generate a large number of microcracks during the loading process. The damage evolution process of model specimens can be divided into three stages: no damage stage, stable damage growth stage, and damage failure stage.

## Declarations

**Conflict of interest** The authors declare that they have no conflict of interest.

## References

1. Huang S, Yao N, Ye Y, Cui X (2019) Strength and failure characteristics of rocklike material containing a large-opening crack under uniaxial compression: experimental and numerical studies. Am Soc Civil Eng 19:04019098

2. Huang M, Xiao T (2020) Study on mechanical and deformation characteristics of prefabricated single-crack rock under uniaxial compression. J Changjiang Univ (Nat Sci Edit) 17:115–120

3. Huang Y, Yang S, Ju Y, Zhou X et al (2016) Experimental study on mechanical properties of intermittent crack-like rock materials under triaxial compression. J Geotech Eng 38:1212–1220. https://doi.org/10.11779/CJGE201607007

4. Wu W, He G, Chen K, Xue Y et al (2021) Fracture test and analysis of rock specimens with noncoplanar intermittent fractures. Nonferrous Metal Eng 11:107–116

5. Chen L, Guo W, Zhang D, Zhao T (2022) Experimental study on the influence of prefabricated fissure size on the directional propagation law of rock type-I crack. Int J Rock Mech Min 160:105274. https://doi.org/10.1016/j.ijrmms.2022.105274

6. Liu X, Zhang K, Li N, Qi F, Ye J (2021) Quantitative identification of fracture behavior of 3D printed rock specimens with holes and double fractures. Rock Soil Mech 42:3017–3028. https://doi.org/10.16285/j.rsm.2021.0521

7. Wang C, Luo X, Chen K, Dai B, He G (2020) Experimental study on fracture evolution and fracture characteristics of rocks containing pre-fabricated fractures. Gold Sci Technol 28:421–429

8. Quan D (2022) Rock compression-shear mechanical test and damage-fracture evolution mechanism research. Guizhou University, p 95

9. Wang E (2019) PFC3D particle flow simulation of mechanical properties of saturated dense silty sand. Nanchang University, p 114

10. Xiao F (2021) Study on mechanical characteristics and failure mechanism of damaged sandstone under true triaxial unloading. Chongqing University, p 154

11. Li Z, Tian H, Niu Y, Wang E, Zhang X, He S, Wang F, Zheng A (2022) Study on the acoustic and thermal response characteristics of coal samples with various prefabricated crack angles during loaded failure under uniaxial compression. J Appl Geophys 200:104618. https://doi.org/10.1016/j.jappgeo.2022.104618

12. Lin H, Yang H, Wang Y, Zhao Y, Cao R (2019) Determination of the stress field and crack initiation angle of an open flaw tip under uniaxial compression. Theor Appl Fract Mech 104:102358. https://doi.org/10.1016/j.tafmec.2019.102358

13. Wang X, Li J, Zhao X, Liang Y (2022) Propagation characteristics and prediction of blast-induced vibration on closely spaced rock tunnels. Tunn Undergr Space Technol 123:104416

14. Linlin Gu, Wei Z, Wenxuan Z et al (2022) Liquefaction-induced damage evaluation of earth embankment and corresponding countermeasure. Front Struct Civ Eng 16(9):1183–1195

15. Huang M, Tang C, Liang Z (2001) Stress field analysis of rock crack interaction. J Northeast Univ 22:446–449. https://doi.org/10.3321/j.issn:1005-3026.2001.04.025

16. Pan P, Zhou H, Feng X (2008) Study on the influence of loading conditions on the uniaxial compression fracture process of rocks with different sizes. J Rock Mech Eng 27:3636–3642. https://doi.org/10.3321/j.issn:1000-6915.2008.z2.049

17. Wang G, Yu G, Gao L, Li G (2017) Study on the influence of initial crack inclination on rock damage and fracture characteristics. Coal Sci Technol 45:100–104

18. Zhang D, Guo W, Zhao T, Zhao Y, Chen Y, Zhang X (2022) Energy evolution law during failure process of coal-rock combination and roadway surrounding rock. Minerals-Basel 12:1535. https://doi.org/10.3390/min12121535

19. He C, Mishra B, Shi Q, Zhao Y, Lin D, Wang X (2023) Correlations between mineral composition and mechanical properties of granite using digital image processing and discrete element method. Int J Min Sci Technol. https://doi.org/10.1016/j.ijmst.2023.06.003

20. Chen Y, Liu H, Yin F, Cui Y, Liu H (2019) Study on the law of crack propagation of rock with cross joints. J Shandong Univ Archit 34:22–26. https://doi.org/10.12077/sdjz.2019.02.004

21. Zhao P, Li S (2019) Crack propagation and material characteristics of rocklike specimens subject to different loading rates. Am Soc Civil Eng 31:04019113

22. Xie L, Jin P, Su T, Li X, Liang Z (2020) Numerical simulation of uniaxial compression tests on layered rock specimens using the discrete element method. Comput Part Mech 7:753–762. https://doi.org/10.1007/s40571-019-00307-3

23. Wang H, Gao Y, Zhou Y (2022) Experimental and numerical studies of brittle rock-like specimens with unfilled cross fissures under uniaxial compression. Theor Appl Fract Mech 117:103167. https://doi.org/10.1016/j.tafmec.2021.103167

24. Zhang W, Chen Y, Guo J, Wu S, Yan C (2021) Investigation into macro- and microcrack propagation mechanism of red sandstone under different confining pressures using 3D numerical simulation and CT verification. Geofluids 2021:1–12. https://doi.org/10.1155/2021/2871687

25. Dong J (2020) Triaxial mechanical properties and particle flow simulation of granite with different grain sizes after high temperature. China University of Mining and Technology, p 126

26. Teng M (2022) Study on shear failure characteristics of rock-like materials with built-in three-dimensional cracks. Guizhou University, p 96

27. Meng F, Song J, Yue Z, Zhou H, Wang X, Wang Z (2022) Failure mechanisms and damage evolution of hard rock joints under high stress: insights from PFC2D modeling. Eng Anal Bound Elem 135:394–411. https://doi.org/10.1016/j.enganabound.2021.12.007

28. Wang G, Feng J, Huang Q, Li S, Chen X, Han D (2022) Theoretical and experimental evaluation of water injection difficulty based on coal structure characteristics. Fuel 326:124932. https://doi.org/10.1016/j.fuel.2022.124932

29. Li BQ, Gonçalves Da Silva B, Einstein H (2019) Laboratory hydraulic fracturing of granite: acoustic emission observations and interpretation. Eng Fract Mech 209:200–220. https://doi.org/10.1016/j.engfracmech.2019.01.034

30. Chen X, Gao W, Hu C, Wang C, Zhou C (2023) Study on macro–micro mechanical behavior of broken rock mass using numerical tests with discrete element method. Comput Part Mech 10:691–705. https://doi.org/10.1007/s40571-022-00521-6

31. Bai Y, Li X, Yang W, Xu Z, Lv M (2022) Multiscale analysis of tunnel surrounding rock disturbance: a PFC3D-FLAC3D coupling algorithm with the overlapping domain method. Comput Geotech 147:104752. https://doi.org/10.1016/j.compgeo.2022.104752

32. Zhu C, An Y, Li W (2022) Study on damage evolution characteristics of transparent rock-like materials under uniaxial compression. Exp Mech 37:701–710. https://doi.org/10.7520/1001-4888-21-267

33. Wangyang L, Chong S, Cong Z (2023) Numerical study on the effect of grain size on rock dynamic tensile properties using PFC-GBM. Comput Part Mech. https://doi.org/10.1007/s40571-023-00634-6

34. Li B, Yu S, Zhu W, Cai W, Yang L, Xue Y, Li Y (2020) The Microscopic mechanism of crack evolution in brittle material containing 3-D embedded flaw. Rock Mech Rock Eng 53:5239–5255. https://doi.org/10.1007/s00603-020-02214-z

35. Chen B, Shen B, Zhang S, Li Y, Jiang H (2022) 3D morphology and formation mechanism of fractures developed by true triaxial stress. Int J Min Sci Technol 32:1273–1284. https://doi.org/10.1016/j.ijmst.2022.09.002

36. Ding F, Song L, Yue F (2022) Study on mechanical properties of cement-improved frozen soil under uniaxial compression based on discrete element method. Processes 10:324. https://doi.org/10.3390/pr10020324

37. Cong Y (2012) Test and PFC3D simulation study of marble loading and unloading failure process. Qingdao Technological University, p 65

38. Chen Y (2020) Study on mechanical properties of sand, mudstone and their interfaces under dry-wet cycles. Chongqing Jiaotong University, p 127

39. Rong H, Li G, Liang D, Xu J, Hu Y (2022) Particle flow simulation of mechanical properties of high stress rock under the influence of stress path. J Min Saf Eng 39:163–173. https://doi.org/10.13545/j.cnki.jmse.2021.0191